

Understanding star formation and feedback in small galaxies[★]

The case of the blue compact dwarf Mrk 900

L. M. Cairós¹ and J.N. González-Pérez²

¹ Institut für Astrophysik, Georg-August-Universität, Friedrich-Hund-Platz 1, D-37077 Göttingen, Germany
e-mail: luzma@astro.physik.uni-goettingen.de

² Hamburger Sternwarte, Gojenbergsweg 112, 21029 Hamburg
e-mail: jgonzalezperez@hs.uni-hamburg.de

Received ...; accepted ...

ABSTRACT

Context. Low-luminosity, active star-forming blue compact galaxies (BCGs) are excellent laboratories for investigating the process of star formation on galactic scales and to probe the interplay between massive stars and the surrounding interstellar (or intergalactic) medium.

Aims. We investigate the morphology, structure, and stellar content of BCG Mrk 900, as well as the excitation, ionization conditions, and kinematics of its H II regions and surrounding ionized gas.

Methods. We obtained integral field observations of Mrk 900 working with the Visible Multi-Object Spectrograph at the Very Large Telescope. The observations were taken in the wavelength range 4150-7400 Å covering a field of view of 27'' × 27'' on the sky with a spatial sampling of 0''.67. From the integral field data we built continuum, emission, and diagnostic line ratio maps and produced velocity and velocity dispersion maps. We also generated the integrated spectrum of the major H II regions and the nuclear area to determine reliable physical parameters and oxygen abundances. Integral field spectroscopy was complemented with deep broad-band photometry taken at the 2.5 m NOT telescope; the broad-band data, tracing the galaxy up to radius 4 kpc, allowed us to investigate the properties of the low surface brightness underlying stellar host.

Results. We disentangle two different stellar components in Mrk 900: a young population, which resolves into individual stellar clusters with ages ~5.5-6.6 Myr and extends about 1 kpc along the galaxy minor axis, is placed on top of a rather red and regular shaped underlying stellar host, several Gyr old. We find evidence of a substantial amount of dust and an inhomogeneous extinction pattern, with a dust lane crossing the central starburst. Mrk 900 displays overall rotation, although distorted in the central, starburst regions; the dispersion velocity map is highly inhomogeneous, with values increasing up to 60 km s⁻¹ at the periphery of the SF regions, where we also find hints of the presence of shocks. Our observational results point to an interaction or merger with a low-mass object or infalling gas as plausible trigger mechanisms for the present starburst event.

Conclusions.

Key words. galaxies – individual: Mrk 900 – dwarf – starburst – stellar populations – star formation

1. Introduction

Blue compact galaxies (BCGs) are low-luminosity ($M_B \geq -18$) and small systems (starburst radius ≤ 1 kpc) that form stars at unusually high rates (up to $3 M_\odot \text{ yr}^{-1}$; Thuan & Martin 1981; Cairós et al. 2001b,a; Fanelli et al. 1988; Hunter & Elmegreen 2004). They are also rich in gas ($M_{\text{HI}} = 10^8 - 10^9 M_\odot$) and present low metal abundances, as derived from their warm ionized gas ($1/40 Z_\odot \leq Z \leq 1/2 Z_\odot$; Thuan et al. 1999; Salzer et al. 2002; Izotov & Thuan 1999; Kunth & Östlin 2000). These characteristics make them excellent targets for investigating the process of star formation (SF) in galaxies:

First, the lack of spiral density waves and strong shear forces (the mechanisms assumed to trigger and maintain SF in spirals; Shu et al. 1972; Nelson & Matsuda 1977; Seigar & James 2002) allow us to investigate the SF process in a relatively simple environment and to search for alternative trigger mechanisms (Hunter 1997); for instance, there is evidence that feedback from

massive stars could be responsible for the ongoing starburst in several BCGs (Cairós & González-Pérez 2017a,b).

Second, the impact of massive stars into the interstellar medium (ISM) of a low-mass galaxy can be dramatic: as the blast-waves created by supernova (SN) explosions propagate, they give rise to huge expanding shells (McCray & Kafatos 1987), which in the absence of density waves and shear forces grow to larger sizes and live longer than in typical spirals. Observations of dwarf star-forming galaxies reveal ionized gas structures stretching up to kiloparsec scales (Hunter & Gallagher 1990; Marlowe et al. 1995; Bomans et al. 1997, 2007; Martin 1998; Cairós et al. 2001a, 2015). In a shallow potential well these expanding shells can break out of the galaxy disk, or even the halo, and can vent the SN enriched material into the ISM and/or intergalactic medium (IGM; Dekel & Silk 1986; Marlowe et al. 1995; Martin 1998, 1999; Mac Low & Ferrara 1999).

Finally, the low metal content and high star formation rate (SFR) of BCGs give us the opportunity to characterize starburst events that are taking place in conditions very similar to those of

[★] Based on observations made with ESO Telescopes at Paranal Observatory under program ID 079.B-0445.

Table 1. Basic parameters of Mrk 900

Parameter	Data	Reference
Other names	NGC 7077, UGC 11755	
RA (J2000)	21 ^h 29 ^m 59 ^s .6	
DEC (J2000)	02°24′51″	
V_{hel}	1152±5 km s ⁻¹	
Distance	18.9±1.3 Mpc	
Scale	91 pc arcsec ⁻¹	
D_{25}	49.9±0.06″ (4.54 kpc)	RC3
A_B	0.211	SF11
M_B	-17.07	This work
M_*	9.5×10 ⁸ M _⊙	H17
M_{HI}	1.55×10 ⁸ M _⊙	VSS01
M_{DYN}	1.64×10 ⁹ M _⊙	VSS01
D_{HI}/D_{25}	1.2	VSS01
Morphology	SO ⁻ pec?; BCD	RC3; GP03

Notes: RA, DEC, heliocentric velocity, distance, scale, and Galactic extinction are from NED (<http://nedwww.ipac.caltech.edu/>). The distance was calculated using a Hubble constant of 73 km s⁻¹ Mpc⁻¹, and taking into account the influence of the Virgo Cluster, the Great Attractor, and the Shapley supercluster. HI-to-optical diameter (D_{HI}/D_{25}) is measured at the 10²⁰ atoms cm⁻² and 25 mag arcsec⁻² isophotes. References: GP03 = Gil de Paz et al. (2003); H17=Hunt et al. (2017); RC3= de Vaucouleurs et al. (1991); SF11=Schlafly & Finkbeiner (2011); VSS01=van Zee et al. (2001).

the early Universe (Madden et al. 2006, 2013; Lebouteiller et al. 2017).

Motivated by the relevance of these topics we initiated a project focused on BCGs and, in particular, on their current starburst episode and the impact on the ISM. To this end we took integral field spectroscopy (IFS) of a sample of forty galaxies. The first results from our analysis are presented in Cairós et al. (2009b,a, 2010, 2012, 2015). A complete understanding of the SF process in low-mass systems and on the complex interaction of massive stars with their environment demand also detailed analyses of individual objects (Cairós & González-Pérez 2017a,b). Here we focus on the BCG Mrk 900 and combine IFS observations with optical imaging to investigate its recent SF and evolutionary history.

Mrk 900 (NGC 7077) is a relatively luminous BCG ($M_B=-17.08$; this work), included in the Mazzarella & Balzano (1986) catalog of Markarian galaxies. Surface photometry in the optical and near-infrared (NIR) revealed a blue starburst on top of a redder regular host (Doublier et al. 1997, 1999; Gil de Paz et al. 2003; Gil de Paz & Madore 2005; Micheva et al. 2013a; Janowiecki & Salzer 2014). Cairós et al. (2015) investigated the starburst component of Mrk 900 by means of IFS: the galaxy emission-line maps showed that SF occurs in various knots, aligned on a southeast–northwest axis, with the largest H II region displaced northwest. The distinct morphology in continuum maps, which peaks at the galaxy center are suggestive of different episodes of SF. In addition, holes and filaments in the ionized gas, together with strong low-ionization lines ([O I] $\lambda 6300$ and [S II] $\lambda \lambda 6717, 6731$) revealed an important impact of the SF on the surrounding ISM and suggest the presence of shocks. For all these reasons Mrk 900 appears to be an ideal target for a thorough study of the effect of SF on the ISM of a dwarf galaxy.

Table 2. Log of the observations

Date	Tel.	Inst.	Grism/Filter	Exp. (s)	Seeing (″)
Aug. 2005	NOT	ALFOSC	B	2700	0.8
Aug. 2005	NOT	ALFOSC	V	2700	0.6
Aug. 2005	NOT	ALFOSC	R	2700	0.7
Aug. 2007	VLT	VIMOS	HR-Blue	4320	0.9-1.4
Aug. 2007	VLT	VIMOS	HR-Orange	4320	0.5-0.9

Notes: The columns list, respectively, observation date, telescope and instrument used, grism or filter, total exposure time and seeing.

2. Observations and data processing

We carried out a spectrophotometric analysis of the BCG Mrk 900. The galaxy central starburst was studied by means of IFS, whereas deep broad-band imaging in the optical was used to derive the properties of the underlying host galaxy. Details of the observations are provided Table 2.

2.1. Broad-band imaging

Broad-band observations of Mrk 900 were carried out in August 2005 with the Nordic Optical Telescope (NOT) at Observatorio del Roque de los Muchachos (ORM) in La Palma. The telescope was equipped with ALFOSC (Andalucía Faint Object Spectrograph and Camera), which provided a field of view (FoV) of 6.5′×6.5′ and a scale of 0.188″ pix⁻¹. We collected CCD images through the *B*, *V*, and *R* filters. We observed under excellent weather conditions: the seeing varied between 0.6 and 0.8 arcsec and the night was photometric.

Image processing was carried out using standard IRAF¹ procedures. Each image was corrected for bias, using an average bias frame, and was flattened by dividing by a mean twilight flat-field image. The average sky level was estimated by computing the mean value within several boxes surrounding the object, and subtracted out as a constant. The frames were then registered (we took a set of three dithered exposures for each filter) and combined to obtain the final frame, with cosmic ray events removed and bad pixels cleaned out. Flux calibration was performed through the observation of photometric stars from the Landolt (1992) list.

2.2. Integral field spectroscopy

Spectrophotometric data of Mrk 900 were collected at the Very Large Telescope (VLT; ESO Paranal Observatory, Chile), working with the *Visible Multi-Object Spectrograph* (VIMOS; Le Fèvre et al. 2003) in its integral field unit (IFU) mode. The observations were done in Visitor Mode in August 2007 with the blue (HR-Blue) and orange (HR-Orange) grisms in high-resolution mode (dispersion of 0.51 Å pix⁻¹ in the wavelength range of 4150–6200 Å, and dispersion of 0.60 Å pix⁻¹ in the range 5250–7400 Å). A field of view (FoV) of 27″×27″ on the sky was mapped with a spatial sampling of 0″.67. The weather conditions were good (see Table 2), and galaxy exposures were

¹ The Image Reduction and Analysis Facility (IRAF) is a software system for the reduction and analysis of astronomical data. It is distributed by the NOAO, which is operated by the Association of Universities for Research in Astronomy, Inc., under cooperative agreement with the National Science Foundation

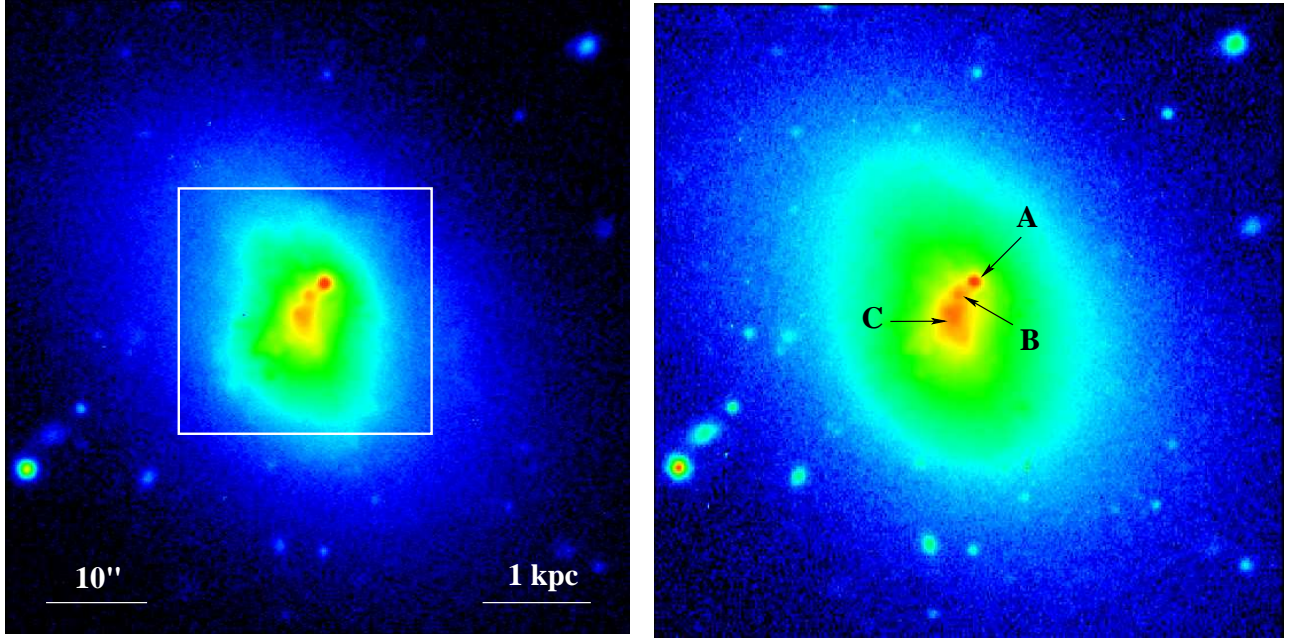


Fig. 1. Broad band images of Mrk 900. Left: B-filter image; the FoV is $\sim 1.0' \times 1.0'$ ($5.5 \times 5.5 \text{ kpc}^2$) and the central box indicates the $27'' \times 27''$ ($2.5 \times 2.5 \text{ kpc}^2$) VIMOS FoV. Right: R-band image (same FoV), with the central major stellar clusters marked. North is up and east to the left.

taken at airmass 1.12-1.21. The spectrophotometric standard EG 274 was observed for flux calibration.

Data were processed using the ESO VIMOS pipeline (version 2.1.11) via the graphical user interface *GASGANO*. The observations and a complete description of the data reduction are presented in Cairós et al. (2015).

2.2.1. Emission-line fitting

The next step in the IFS data process is the measurement of the fluxes in emission lines, required to produce the bidimensional galaxy maps. We computed the fluxes by fitting Gaussians to the line profiles. The fit was performed using the task `fit` of *MATLAB* with the *Trust-region* algorithm for nonlinear least squares. We ran an automatic procedure, which fits a series of lines for every spaxel, namely, $\text{H}\beta$, $[\text{O III}] \lambda 4959$, $[\text{O III}] \lambda 5007$, $[\text{O I}] \lambda 6300$, $\text{H}\alpha$, $[\text{N II}] \lambda 6584$ and $[\text{S II}] \lambda \lambda 6717, 6731$. For each line the fitting task provides the flux, the centroid position, the line width and continuum, and the corresponding uncertainties of each parameter; 1σ errors are computed by the task using the inverse factor from QR decomposition of the Jacobian, the degrees of freedom, and the root mean square. After carefully inspecting the data, in particular in regions with constant emission-line fluxes, we found that the errors given by the fitting task seem underestimated. Therefore, we increased the errors of the emission-line fluxes by multiplying by 1.34, a factor that matches the spatial variations of the fluxes.

Line profiles were fitted using a single Gaussian in all but the Balmer lines. Determining accurate fluxes of the Balmer emission lines is not straightforward since these fluxes can be significantly affected by stellar absorption (McCall et al. 1985; Olofsson 1995; González Delgado et al. 1999). To take this ef-

fect into account, we applied two different methods depending on the characteristics of the individual profile. If the absorption wings were clearly visible (as was often the case in $\text{H}\beta$), we used two Gaussians, one in emission and one in absorption, and derived the fluxes in absorption and emission simultaneously. In the absence of clear visible absorption wings, a reliable decomposition is impossible (this is often the case with $\text{H}\alpha$), and we assumed that the equivalent width in absorption in $\text{H}\alpha$ was the same as in $\text{H}\beta$; this is well supported by the predictions of the models (Olofsson 1995; González Delgado et al. 1999).

In low surface brightness (LSB) regions a spatial smoothing procedure was applied to increase the accuracy of the fit. Depending on the signal-to-noise ratio (S/N), the closest 5, 9, or 13 spaxels were averaged before the fit was carried out. In this way, we maintain the spatial resolution of the bright regions of the galaxy while obtaining a reasonable S/N for the faint parts, but with a lower spatial resolution.

2.2.2. Creating the galaxy maps

The parameters of the line fits were used subsequently to construct the 2D maps, taking advantage of the fact that the combined VIMOS data are arranged in a regular 44×44 matrix.

Continuum maps in different spectral ranges were obtained by integrating the flux in specific spectral windows, selected so as to avoid strong emission lines or residuals from the sky spectrum subtraction. We also built an integrated continuum-map by integrating over the whole spectral range, but masking the spectral regions with a significant contribution of emission lines.

Line ratios maps for lines falling in the wavelength range of either grism were computed by dividing the corresponding flux maps. In the case of $\text{H}\alpha/\text{H}\beta$, the line ratio map was derived after

registering and shifting the $H\alpha$ map to spatially match the $H\beta$ map. The shift was calculated using the difference in position of the center of the brighter HII regions. The shift was applied using a bilinear interpolation. In order to correct for the fact that $H\alpha$ and $H\beta$ had been observed under different seeing conditions, the $H\alpha$ map was degraded convolving with a Gaussian to match both PSFs.

Only spaxels with a flux level higher than the 3σ level were considered when building the final maps. All maps were corrected for interstellar extinction in terms of spaxels applying Eq. 2 (see Sect. 3.4).

3. Results

3.1. Broad-band morphology: a first view on the stars

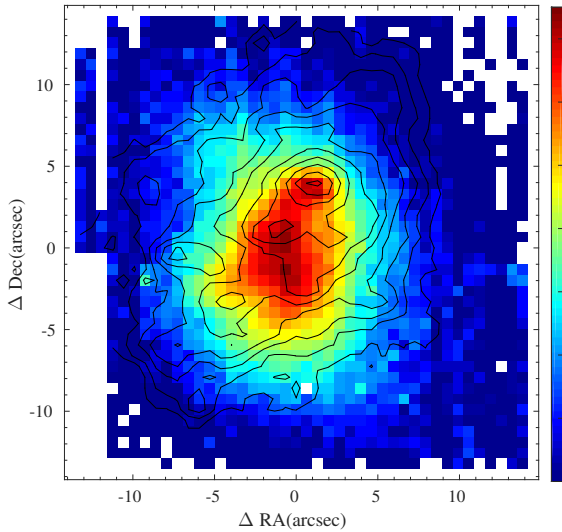


Fig. 2. Mrk 900 continuum map from the VIMOS/IFU data built by summing over the whole blue spectral range (4150–6200 Å), but masking the emission lines. Contours in $H\alpha$ are overplotted. The scale is logarithmic and the units are arbitrary. The FoV is $\sim 2.5 \times 2.5$ kpc², with a spatial resolution of about 61 pc per spaxel. North is up and east to the left; the axes represent the displacements in RA and DEC with respect to the center of the FoV, also in all the maps presented from here on.

The NOT B and R frames of Mrk 900 are presented in Figure 1. In the full ALFOSC FoV the irregular high surface brightness (HSB) region is very well distinguished on top of the low surface brightness (LSB) host. The HSB area is resolved into three major knots (A, B, and C in Figure 1); the emission peaks at the position of the knot A (the clump displaced northwest), while knot C is situated roughly at the center of the redder host. The VIMOS continuum map (Fig. 2) essentially reproduces the same morphological pattern of the galaxy in broad-band frames, but with a notable difference: in continuum the intensity peaks at the position of knot C, and knot A is just a moderate emitter. We masked strong emission lines when constructing the VIMOS continuum map; however, broad-band filters also encompass the

Table 3. Integrated photometry and structural parameters of Mrk 900.

Parameter	B	V	R
m (mag)	14.30±0.03	13.68±0.04	13.35±0.03
M (mag)	-17.08	-17.70	-18.03
$\mu_{0,host}$ (mag arcsec ⁻²)	21.60±0.10	20.87±0.10	20.20±0.06
α_{host} (pc)	726±25	754±24	673±13
m_{host} (mag)	14.89	14.12	13.73
M_{host} (mag)	-16.49	-17.26	-17.65

Notes. Integrated magnitudes computed from the flux within the isophote at 26.5 mag per arcsec⁻². Structural parameters of the exponential disk model best fitting the underlying host galaxy and integrated and absolute magnitudes of the host; all magnitudes are corrected from Galactic extinction following Schlafly & Finkbeiner (2011).

emission from the ionized gas². The much higher intensity of knot A in broad-band filters compared with the continuum indicates that a significant part of its light originates in the ionized gas and reveals the presence of ionizing (very young) stars.

We built the galaxy color maps (i.e., the ratio of the flux emitted in two different filters). We computed the maps from the flux calibrated broad-band images after they were aligned and matched to the same seeing. In order to improve the S/N in the outer galaxy regions, we applied a circular-averaging filter to the individual images, the radius of the filter depending on the flux level in the R band; the filtering is only implemented at large radius ($\geq 10''$), so that the spatial resolution in the central HSB regions is preserved. To avoid artifacts we did not remove foreground stars from the field.

Two major stellar components are clearly distinguished in the $(B-R)$ color map of Mrk 900 (Figure 3). The HSB region appears distorted and much bluer (most probably the result of one or more episodes of SF), while the host galaxy shows a smooth elliptical shape with a markedly redder color. There is an apparent color gradient among the major central knots: $(B-R) \sim 0.23, 0.56,$ and 0.64 in knots A, B, and C, respectively, corrected from Galactic extinction following Schlafly & Finkbeiner (2011). We find for the galaxy host a roughly constant $(B-R) \sim 1.21$, in good agreement with the color profiles reported by Gil de Paz et al. (2003) and Micheva et al. (2013a).

3.2. Integrated and surface brightness photometry

The photometry of Mrk 900 is presented in Table 3. We computed the integrated magnitudes as the magnitudes within the isophote at surface brightness 26.5 mag arcsec⁻² in the B band, namely the Holmberg isophote. We corrected for Galactic extinction using the reddening coefficients from Schlafly & Finkbeiner (2011).

We also built the galaxy surface brightness profiles (SBPs). There are many studies on surface brightness photometry of BCGs (Papaderos et al. 1996, 2002; Doublier et al. 1997, 1999; Cairós et al. 2001a; Noeske et al. 2003, 2005; Gil de Paz & Madore 2005; Caon et al. 2005; Micheva et al. 2013a,b; Janowiecki & Salzer 2014). As pointed out in most of them, the construction of the SBP of a BCG is not straightforward; the most common methods assume some sort of galaxy symmetry and do not necessarily apply to the irregular HSB region of a BCG (Papaderos et al. 1996, 2002; Doublier et al.

² The B-band filter is mostly affected by the $H\gamma$ and $H\beta$ lines, whereas the emission from $H\alpha$, [SII], and [NII] fall in the R band.

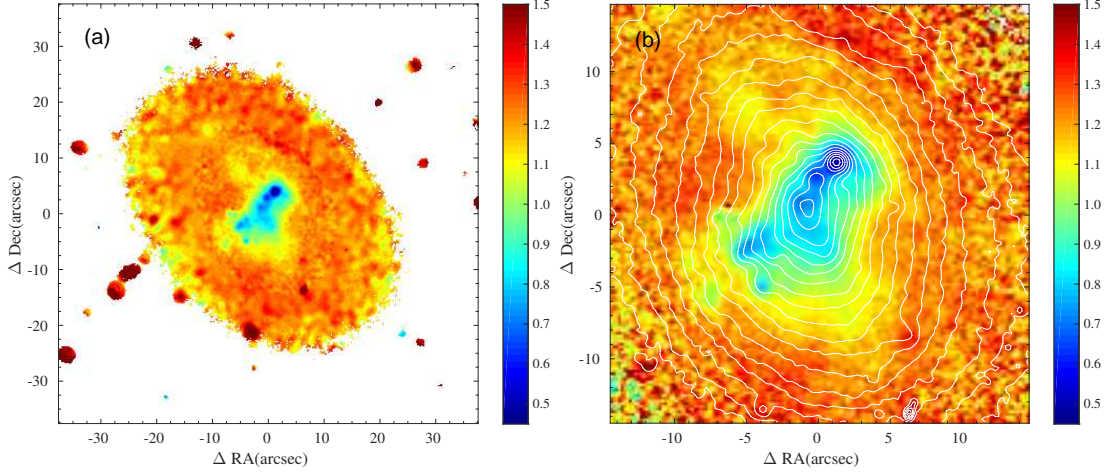


Fig. 3. (a) $(B - R)$ color map of Mrk 900 derived from the NOT frames. (b) Zoomed-in image of the central $27'' \times 27''$ (VIMOS FoV) of the $(B - R)$ color map, with the R-band contours overlaid.

1997; Cairós et al. 2001b; Noeske et al. 2003, 2005). A simple way to overcome this problem is to construct the profile using different approaches in the high- and low-intensity regimes; in the brighter regions, a method that does not require any assumption on the galaxy morphology is used, whereas ellipses are fitted to the isophotes of the smooth host (Cairós et al. 2001b).

Here we opted to build the light profiles using standard techniques, but bearing in mind that they provide a proper description of the galaxy structure only outside the starburst region, which is easily assessed using the color map (Figure 3). After masking out foreground stars and nearby objects, we fitted elliptical isophotes to the images using the IRAF task *ellipse* (Jedrzejewski 1987). The fit was done in two steps: first, the parameters of the ellipses were left free to vary; in a second run, and to improve the stability of the final fit, we fixed the center to the average center of the outer isophotes found in the first step. We found that at large radius ($20'' \leq r \leq 40''$) the galaxy isophotes are well fitted with ellipses of position angle $PA=40^\circ$ and ellipticity $\epsilon=0.30$, in good agreement with the values $PA=41^\circ$ and $\epsilon=0.27$ reported by Micheva et al. (2013a).

The SBPs of Mrk 900 in B , V , and R are displayed in Figure 4. The error bars on the surface brightness magnitudes were calculated taking into account the errors given by the fit and the errors on the estimation of the sky value. The profiles show the common behavior among BCGs: there is a brightness excess in the inner region, but at large radii the intensity seems well described by an exponential decay.

We fitted an exponential disk to the outer profile to obtain the structural parameters of the underlying host galaxy. We performed a weighted linear least-squares fit to the function

$$\mu(r) = \mu_0 + 1.086 \frac{r}{\alpha}, \quad (1)$$

where $\mu(r)$ is the observed surface brightness at radius r , μ_0 is the extrapolated central surface brightness, and α is the exponential scale of the disk. A delicate step is the selection of the fitting radial range: the lower radial limit is given by the position where the contribution of the starburst light is negligible, and the higher radius is set by the point where the sky errors are very large or the ellipses parameters unstable; the final values of the parameters are not very sensitive to the higher radius used since the

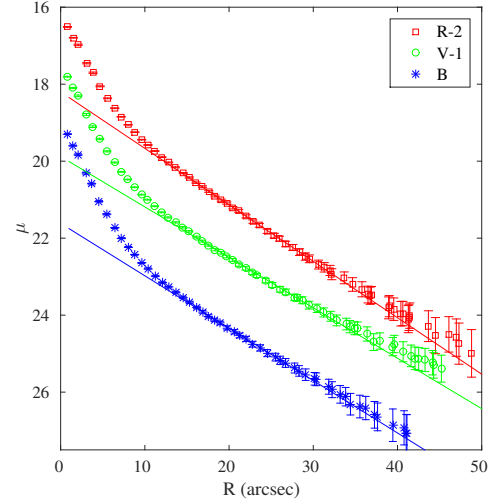


Fig. 4. Surface brightness profiles of Mrk 900 in B , V , and R . For a better visualization the V and R profiles are shifted 1 and 2 magnitudes, respectively. We also plotted the straight lines describing the exponential profile of the underlying host galaxy.

larger errors make the weight of these points to be very low. The structural parameters resulting from the fit in each band (i.e., the central surface brightness, $\mu_{0,host}$, and the scale length, α_{host}) are presented in Table 3. Adopting the disk model, we also computed the integrated and absolute magnitudes of the host galaxy.

3.3. Emission-line maps: warm ionized gas

Emission lines in starburst galaxies trace regions of warm ionized gas, and hence the population of ionizing stars. Mrk 900 shows an irregular morphology in emission lines (see Figures 5-8): several SF knots appear close to the galaxy center and along the minor axis (southeast–northwest). The brightest knot, which spatially coincides with knot A in the broad-band frames, is displaced about 350 pc northwest from the continuum peak (at a distance of 18.9 Mpc the spaxel element translates into 61 pc).

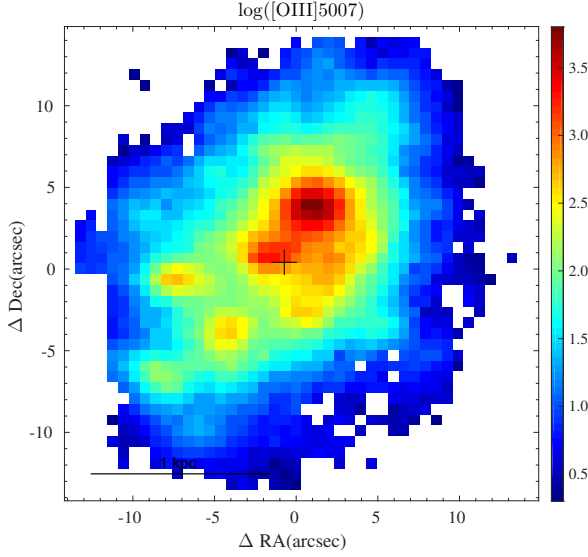


Fig. 5. [O III] $\lambda 5007$ emission-line flux map for Mrk 900, with a cross marking the position of the continuum peak. The spatial scale in pc is indicated at the bottom left; the spatial resolution is about 61 pc per spaxel (91 pc per arcsec) and flux units are $10^{-18} \text{ erg s}^{-1} \text{ cm}^{-2}$, also in all the emission-line maps presented from here on.

These SF regions are embedded in an extended envelope of diffuse ionized gas (DIG), which fills almost the whole FoV. Filaments and curvilinear features are conspicuous at faint brightness levels: the larger ones extend in the SW direction and NE direction. A hole in the warm gas emission, with a diameter of about 260 pc, is visible to the NW close to the biggest SF region.

We adopt here the common definition for the DIG, namely diffuse ionized hydrogen outside the discrete (well-defined) H II regions (Reynolds et al. 1973; Dopita & Sutherland 2003; Oey et al. 2007). To make a clear-cut distinction between spaxels belonging to H II regions and to the DIG is not straightforward (see, e.g., the discussion in Flores-Fajardo et al. 2009). However a substantial fraction of the warm ionized emission in Mrk 900 belong to the DIG according to the currently most used criteria: for instance, the high values of the low-ionization [S II] $\lambda\lambda 6717, 6731/\text{H}\alpha$ line ratio (see Section 3.5 below) and the low values of the $\text{H}\alpha$ equivalent width (Fig. 17) in the outer galaxy regions are characteristic of the DIG following the criteria proposed in Blanc et al. (2009) and Lacerda et al. (2018), respectively.

The galaxy displays the same morphological pattern in all emission lines, but fainter SF clumps appear better delineated in the high-excitation [O III] $\lambda 5007$ line than in the hydrogen recombination lines, and they are only barely visible in the low-ionization [N II] $\lambda 6584$ and [S II] $\lambda\lambda 6717, 6731$ maps.

3.4. Interstellar extinction pattern

The interstellar extinction in a nebulae is computed by comparing the observed Balmer decrement values to the theoretical ones (Osterbrock & Ferland 2006). Since the Balmer line ratios are well known from atomic theory, deviations from the predicted

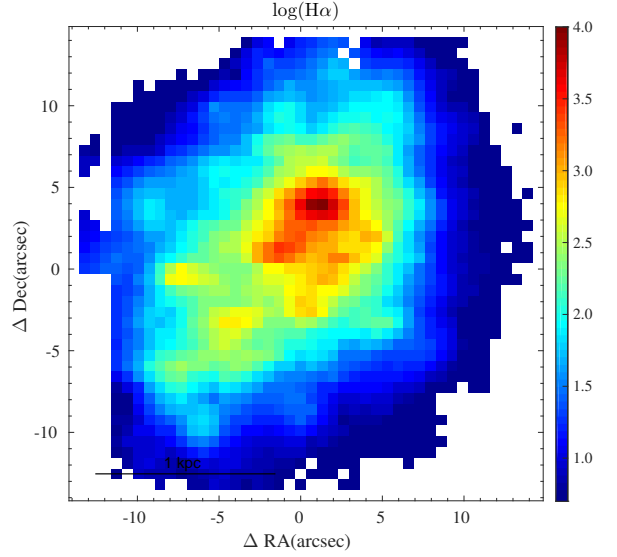


Fig. 6. $\text{H}\alpha$ emission-line flux map for Mrk 900.

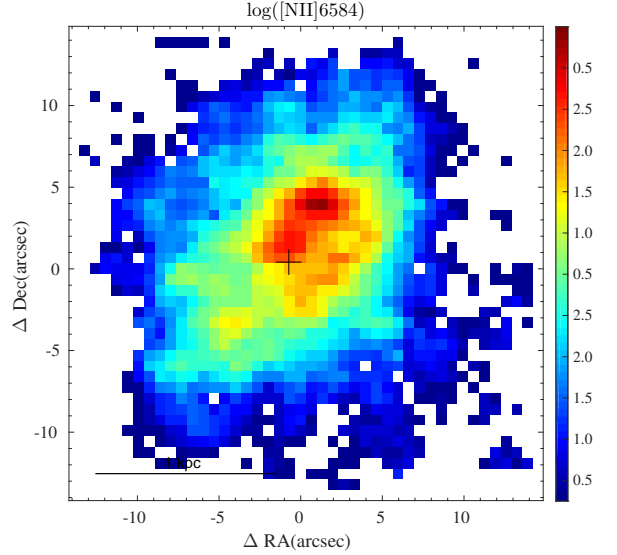


Fig. 7. [N II] $\lambda 6584$ emission-line flux map for Mrk 900.

values are assumed to be due to dust; the interstellar extinction coefficient, $C(\text{H}_\beta)$, is derived as

$$\frac{F_\lambda}{F(\text{H}_\beta)} = \frac{F_{\lambda,0}}{F(\text{H}_{\beta,0})} \times 10^{-C(\text{H}_\beta)[f(\lambda)-f(\text{H}_\beta)]}, \quad (2)$$

where $F_\lambda/F(\text{H}_\beta)$ is the observed ratio of Balmer emission-line intensities relative to H_β , $F_{\lambda,0}/F(\text{H}_{\beta,0})$ the theoretical ratio and $f(\lambda)$ the adopted extinction law. We applied Eq. (2) to every spaxel to obtain an interstellar extinction map (Figure 9).

In practice, we derived the extinction coefficient using only the $\text{H}\alpha/\text{H}_\beta$ ratio; although $\text{H}\gamma$ also falls into the observed wavelength range, it has a poorer S/N and is also more severely affected by underlying stellar absorption compared to H_α and H_β (Olofsson 1995; González Delgado & Leitherer 1999). We adopted case B recombination and low-density limit with a temperature of 10000 K for $F_{\lambda,0}/F(\text{H}_{\beta,0})$ in Eq. (2). We used the

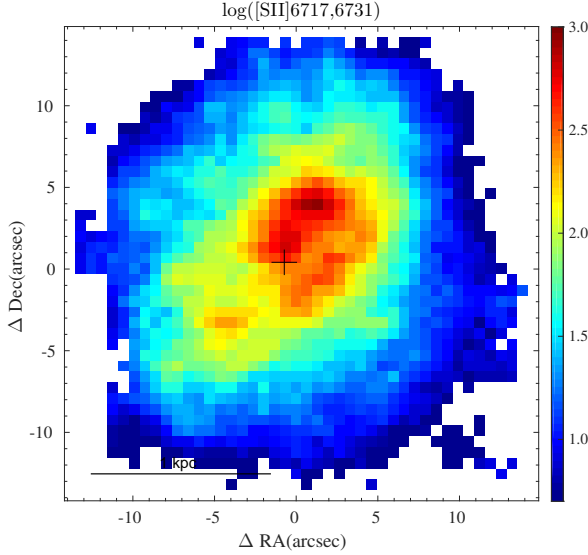


Fig. 8. [S II] $\lambda\lambda 6717, 6731$ emission-line flux map for Mrk 900.

Galactic extinction law from O’Donnell (1994); Mrk 900 is closer in metallicity to the Large Magellanic Cloud (LMC), but differences between the Galactic and the LMC extinction curves are insignificant in the observed spectral range (Dopita & Sutherland 2003).

The interstellar extinction map of Mrk 900 (Figure 9) reveals a clear spatial pattern. The lowest extinction values are reached at the position of the SF regions, and the highest in the inter-knot area. In addition, extinction anticorrelates with the $H\alpha$ intensity: the maximum extinction values are in the regions of fainter $H\alpha$ emission. These results are consistent with dust being destroyed or swept away by the most massive stars.

In the whole FoV, $H\alpha/H\beta \geq 3.5$, which indicates a significant amount of dust even at the position of the SF regions ($H\alpha/H\beta=3.5$ implies an extinction coefficient $C(H\beta)=0.23$ and a color excess $E(B-V)=0.17$). Away from the SF regions, $H\alpha/H\beta$ reaches values up to 6, meaning $C(H\beta)=0.87$ and $E(B-V)=0.64$. Such large spatial variability in the extinction agrees with the results of previous analyses (Lagos et al. 2014; Cairós et al. 2015; Cairós & González-Pérez 2017a,b) and strengthens the conclusions of those works: applying a unique extinction coefficient to the whole galaxy, as usually done for long-slit spectroscopic observations, can lead to large errors in derived fluxes, magnitudes, and SFR.

3.5. Excitation and ionization mechanisms

Specific emission-line ratios, namely [O III] $\lambda 5007/H\beta$, [N II] $\lambda 6584/H\alpha$, [S II] $\lambda\lambda 6717, 6731/H\alpha$, and [O I] $\lambda 6300/H\alpha$, reveal the excitation and ionization mechanisms in a nebula (Dopita & Sutherland 2003; Osterbrock & Ferland 2006); IFU observations enable us to investigate the spatial variations of excitation and ionization conditions in galaxies (Sharp & Bland-Hawthorn 2010; Rich et al. 2011, 2012, 2015; Cairós & González-Pérez 2017a,b; Mingozi et al. 2019).

The [O III] $\lambda 5007/H\beta$ distribution of Mrk 900 (Figure 10) is not uniform, but shows a clear spatial pattern: the highest excitation is reached at the position of the SF regions. This is expected as a harder ionization source ($h\nu \geq 35.1$ eV), such as very

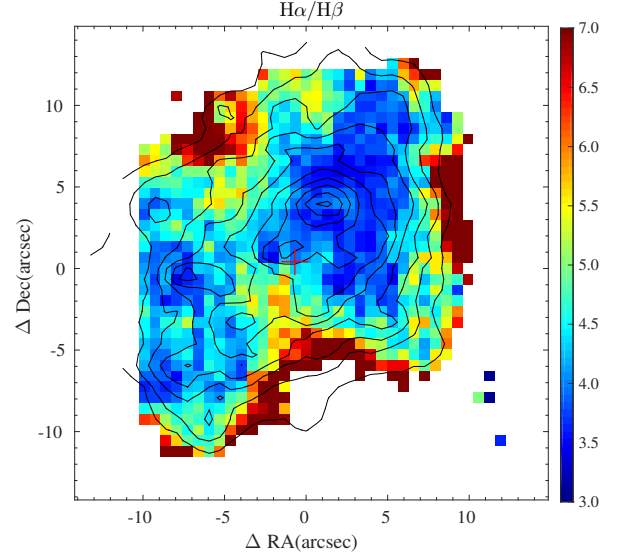


Fig. 9. $H\alpha/H\beta$ ratio map for Mrk 900, with the contours of the $H\alpha$ flux map overlotted.

young O stars, is required to cause a strong [O III] $\lambda 5007$ line. The excitation reaches its maximum at the position of the major $H\alpha$ emitter ([O III] $\lambda 5007/H\beta \sim 3.0$). Interestingly, there are two other zones, not co-spatial with any SF knot, with a relatively high excitation (Figure 10). An enhancement on the excitation in regions not photoionized by stars can be due to the presence of shocks and/or a large amount of dust; the excitation maximum at the south is very close to the peak in interstellar extinction.

The maps for low-ionization species [O I] $\lambda 6300/H\alpha$, [N II] $\lambda 6584/H\alpha$, and [S II] $\lambda\lambda 6717, 6731/H\alpha$ (Figures 11 – 13, respectively) show the opposite behavior, with the line ratios reaching their minimum at the center of the SF knots. This is expected in regions ionized by UV photons coming from massive stars. All three line ratios appreciably increase outward ([S II] $\lambda\lambda 6717, 6731/H\alpha \geq 0.6$), which are values much higher than those predicted for stellar photoionization.

From the emission-line ratio maps, we generated spaxel resolved diagnostic diagrams; we plotted in the classical diagnostic diagrams (Baldwin et al. 1981; Veilleux & Osterbrock 1987) the value of the line ratios at each individual element of spatial resolution. This technique permits us to explore the power sources acting in different galaxy regions (Sharp & Bland-Hawthorn 2010; Rich et al. 2011, 2012, 2015; Leslie et al. 2014; Cairós & González-Pérez 2017a,b).

Figure 14 displays the diagnostic line diagrams for Mrk 900, together with the maximum starburst line (or photoionization line) derived by Kewley et al. (2001); this line traces the limit between gas photoionized by young stars and gas ionized via other mechanisms (AGN or shock excitation). We found that a considerable fraction of the spaxels fall outside of the area occupied by star photoionization in the diagrams [O III] $\lambda 5007/H\beta$ versus [O I] $\lambda 6300/H\alpha$ and [O III] $\lambda 5007/H\beta$ versus [S II] $\lambda\lambda 6717, 6731/H\alpha$. The ratio [N II] $\lambda 6584/H\alpha$, weakly dependent on the hardness of the radiation but strongly dependent on the metallicity, is not effective in separating shocks from photoionized regions. In particular, at low metallicities ($0.2 Z_{\odot} \leq Z \leq 0.4 Z_{\odot}$) this diagram is degenerated, and

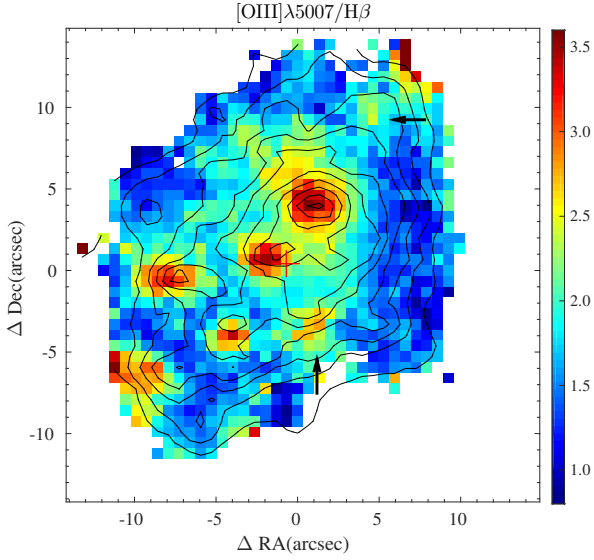


Fig. 10. [O III] $\lambda 5007/H\beta$ emission-line ratio map with contours on $H\alpha$ overplotted. The arrows indicate areas of enhancement of the line ratio, which do not spatially coincide with any SF regions.

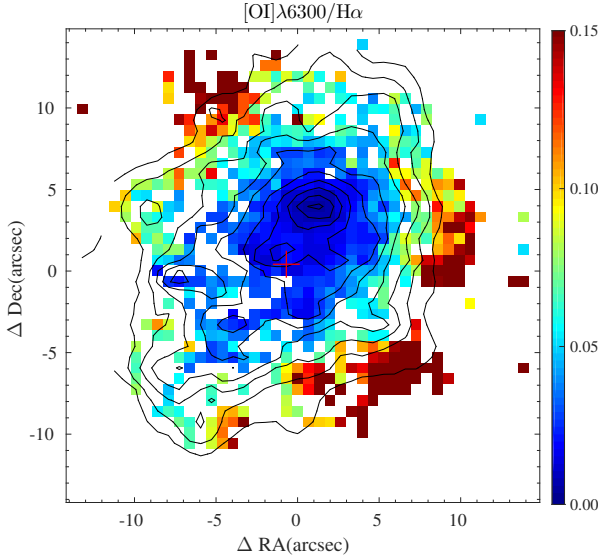


Fig. 11. [O I] $\lambda 6300/H\alpha$ emission-line ratio map with contours on $H\alpha$ overplotted.

shock-ionization and photoionization overlap (Allen et al. 2008; Hong et al. 2013).

In order to better visualize this result, we display the spatial position of these spaxels on the galaxy in Fig. 15. The areas not photoionized are situated mainly at the periphery of the mapped region and in the inter-knot space, which conforms to the idea that they are shocked regions, generated in the interface between the expanding bubbles (produced by the massive stellar feedback) and the ambient ISM. This behavior has also been observed in other BCGs, for example Haro 14 and Tololo 1937-423 (Cairós & González-Pérez 2017a,b), and in dwarf irregu-

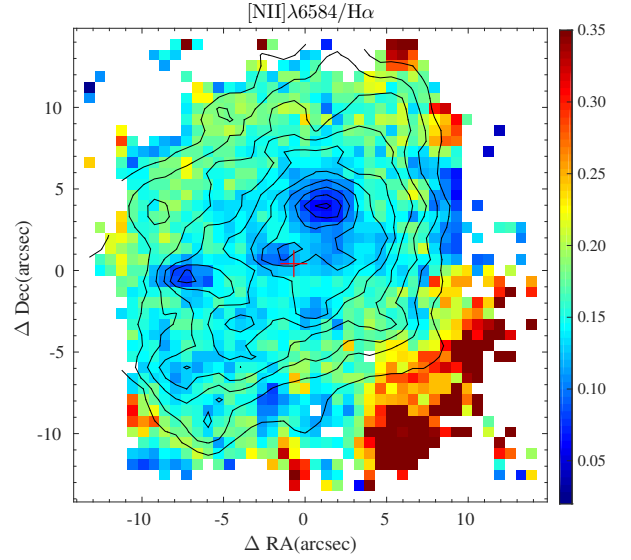


Fig. 12. [N II] $\lambda 6584/H\alpha$ emission-line ratio map with contours on $H\alpha$ overplotted.

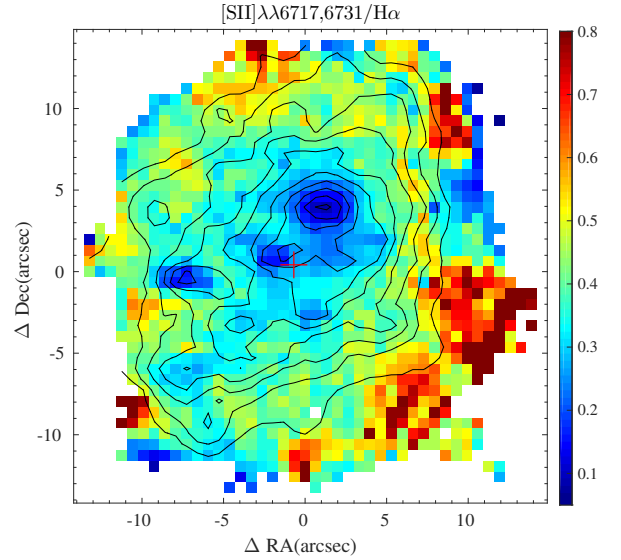


Fig. 13. [S II] $\lambda\lambda 6717, 6731/H\alpha$ emission-line ratio map with contours on $H\alpha$ overplotted.

lar galaxies, for example NGC4449 (Kumari et al. 2017) and NGC 5253 (Calzetti et al. 1999, 2004).

3.6. Ionized gas kinematics

The line-of-sight (LOS) velocity map in $H\alpha$, measured from the Doppler shift of the line profile centroid relative to the galaxy systemic velocity, is shown in Figure 16. A distorted, but ordered rotation field pattern is evident, with the velocity gradient aligned along the optical major axis: the regions situated north-east are moving away from us, while the southwest regions are moving toward us. Deviations from the global rotation are apparent across the whole FoV; particularly interesting is the curvilinear feature in the southwest, spatially coincident with the regions

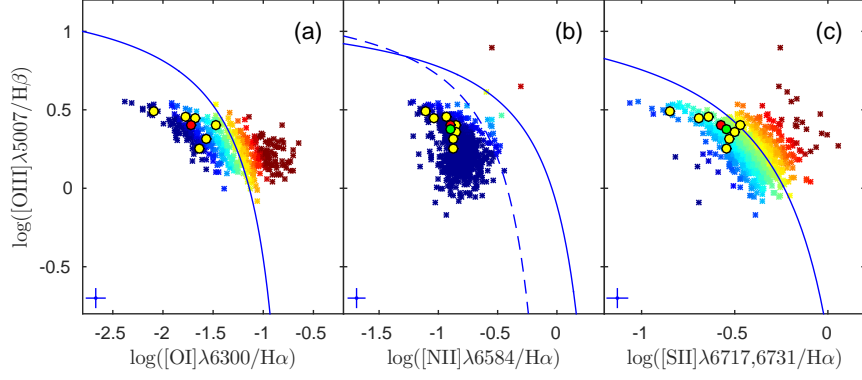


Fig. 14. Optical emission-line diagnostic diagram for the individual spaxels in Mrk 900; the ratio for the SF regions identified in the galaxy and for the nuclear and integrated spectrum are also shown in the plot (yellow, red, and green circles represent the SF regions, the nuclear, and the integrated spectrum, respectively). The solid black line in the panels delineates the theoretical “maximum starburst line” derived by Kewley et al. (2001); the dashed black curve in panel (b) traces the Kauffmann et al. (2003) empirical classification line. To better visualize the results on the diagram, the points are color-coded according to their distance to the maximum starburst line. In both diagrams, the lower-left section of the plot is occupied by spaxels in which the dominant energy source is the radiation from hot stars (blue points in the figure). Additional ionizing mechanisms shift the spaxels to the top right and right part of the diagrams (from yellow to red).

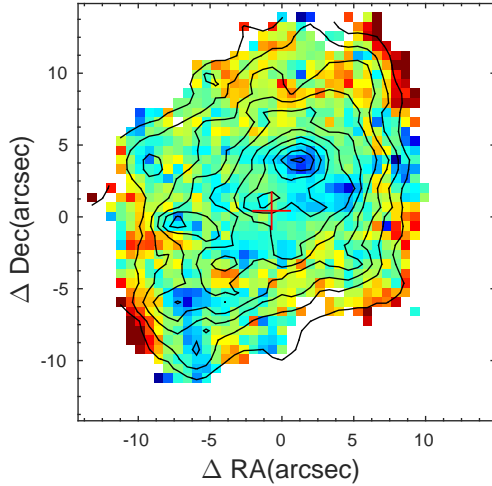


Fig. 15. Spatial localization of the spaxels in the diagnostic diagram $[\text{O III}] \lambda 5007/\text{H}\beta$ vs. $[\text{S II}] \lambda \lambda 6717, 6731/\text{H}\alpha$. The color-coding is the same as in Figure 14. The redder regions are those situated above the maximum starburst line from Kewley et al. (2001).

of enhancement in $[\text{N II}] \lambda 6584/\text{H}\alpha$ and $[\text{S II}] \lambda \lambda 6717, 6731/\text{H}\alpha$ in the diagnostic maps.

The kinematics of Mrk 900 has been studied in the multi-pupil IFS analysis of 18 BCGs by Petrosian et al. (2002). These authors found a homogeneous velocity field in the $\text{H}\alpha$ emission line and excluded the possibility of a strong rotational gradient in the galaxy, but this result clearly arises from their limited FoV. Their velocity map, centered roughly where the continuum peaks, covers about 9.1×13 arcsec; consequently, the whole field is dominated by the starburst emission. Using H I synthesis observations, van Zee et al. (2001) investigated the kinematics of Mrk 900 in a much larger FoV; the overall pattern of their velocity map (see their Figure 6) is in good agreement with our results.

The $\text{H}\alpha$ LOS velocity dispersion, derived from the width of the Gaussian fit to the line profile after accounting for the instrumental (~ 9.9 km/sec) and thermal broadening (~ 9.1 km/s), also shows a clear spatial pattern (Figure 16). The minimum values are reached at the SF knots ($5 \text{ km s}^{-1} \leq \sigma \leq 15 \text{ km s}^{-1}$), while the velocity dispersion increases up to values $\sim 60 \text{ km s}^{-1}$ at the galaxy periphery and in the inter-knot region. A nonuniform spatial distribution has also been found in several BCGs for which 2D maps of the ionized gas velocity dispersion has been published (Bordalo et al. 2009; Moiseev & Lozinskaya 2012; Moiseev et al. 2015; Cairós et al. 2015; Cairós & González-Pérez 2017a,b). Based on this result, Moiseev et al. (2015) claimed that the large velocity dispersions (turbulent motions in the ionized gas) observed in dwarf galaxies do not reflect virial motions, but are instead related to the feedback from young massive stars.

3.7. Integrated spectroscopy

Using the bidimensional maps we identified the major regions of SF in the galaxy. To delimit their borders we used the $\text{H}\alpha$ equivalent width map; equivalent widths of hydrogen recombination lines are excellent age indicators (Dottori 1981; Stasińska & Leitherer 1996; Leitherer 2005; Levesque & Leitherer 2013). The $\text{H}\alpha$ equivalent width map of Mrk 900 (Figure 17) traces the $\text{H}\alpha$ flux, but the H II regions are better delineated and, in particular, various small clumps located at the filaments are conspicuous.

Because there is no clear-cut criterion to set the limits of the knots, we integrated over a boundary tracing the morphology of the cluster, taking into account that we are limited by the seeing. In this way we singled out seven major H II regions in Mrk900 (labeled in Figure 17). We generated the integrated spectrum of each knot by adding the spectra of the corresponding spaxels, so we obtained a higher S/N spectrum compared to those of the individual fibers, more suitable to derive physical parameters and abundances. We also produced the “nuclear” spectrum, adding the signal of the spaxels around the continuum peak, and the total spectrum, adding all the spaxels in the $\text{H}\alpha$ emission line flux map.

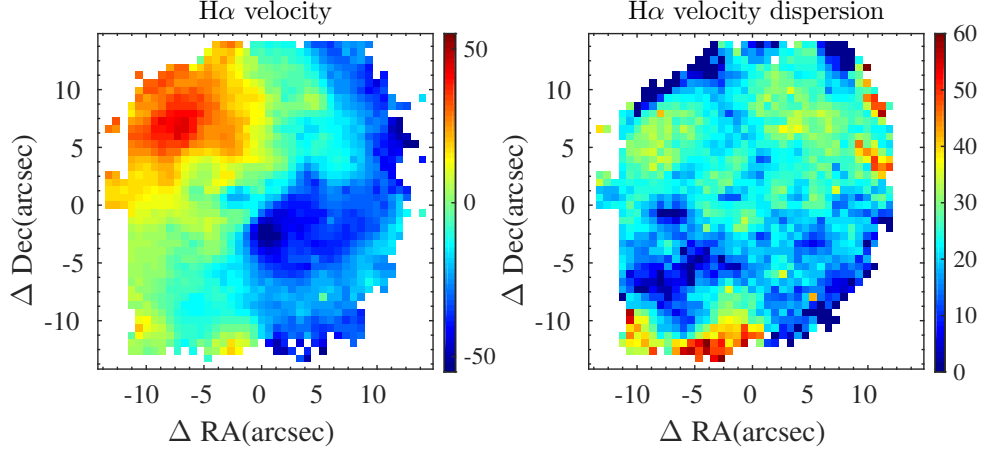


Fig. 16. H α line-of-sight velocity field and velocity dispersion map; shown are velocity and velocity dispersions in km s $^{-1}$.

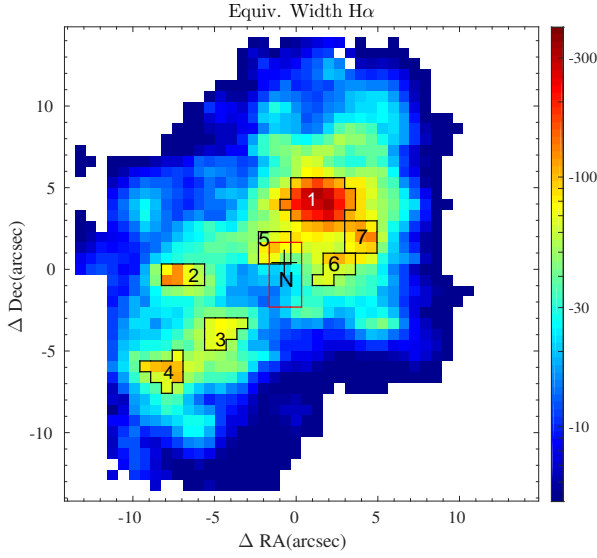


Fig. 17. H α equivalent width map (in Å) for Mrk 900, with the seven major regions of SF labeled.

All SF knots display a typical nebular spectrum, with strong Balmer lines and [OIII], [NII], and [SII] forbidden lines in emission, on top of an almost featureless continuum. As expected, the spectrum of the nuclear region presents a higher continuum and more pronounced absorption features. As an illustration, we show the spectra of three out of the seven SF regions and the nuclear region in Figure 18. In knot 1 we detect the broad-band Wolf-Rayet (WR) bump at $\lambda 4650\text{--}4690$ Å, the unresolved blend of NIII $\lambda 4640$, CIII $\lambda 4650$, CIV $\lambda 4658$, and HeII $\lambda 4686$ Å lines (see Fig. 19; Conti 1991; Schaerer et al. 1999). The S/N of the spectra is too low for a reliable measurement of the WR bump flux, but just the detection of WR stars strongly constrains the age, duration, and initial mass function (IMF) of the SF episode (Meynet 1995; Schaerer & Vacca 1998; Guseva et al. 2000). At the metallicity of Mrk 900 (see Section 3.7.2 below) the presence of WRs is consistent with these stars being formed in an instantaneous burst, with ages between 3 and 6.3 Myr, and an IMF with an upper mass limit of 100 M \odot (Leitherer & Heckman 1995; Leitherer et al. 1999).

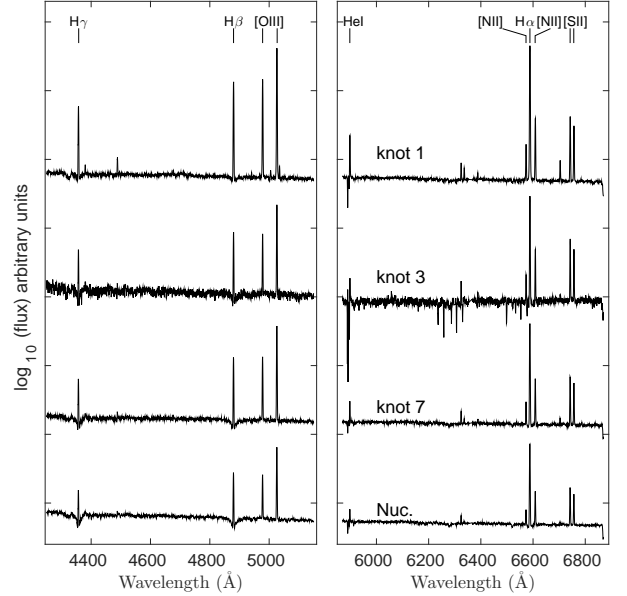


Fig. 18. Flux-calibrated spectra of three of the seven selected H II regions and the nuclear region in Mrk 900, in logarithmic units.

3.7.1. Emission-line fluxes

We measured the observed emission-line fluxes in each of these spectra using the IRAF task *splot*. The contribution of the Balmer lines in absorption was taking into account, as discussed in Section 2.2.2. From the observed Balmer decrement we computed the interstellar extinction coefficient, as explained in Section 3.4. The reddening-corrected intensity ratios are presented in Table 5, together with the derived interstellar extinction coefficient, $C(H\beta)$; for an easier comparison with other data, the number of magnitudes of extinction in V, A_V , and the color excess, $E(B - V)$, are also shown.

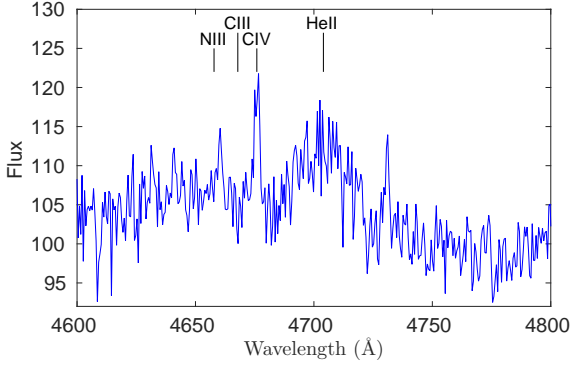


Fig. 19. Enlarged region of the spectrum around blue WR bump ($\lambda 4650 - 4690 \text{ \AA}$) in the knot 1. This feature is attributed to the blends of NIII $\lambda 4640$, CIII $\lambda 4650$, CIV $\lambda 4658$, and HeII $\lambda 4686 \text{ \AA}$ lines.

3.7.2. Diagnostic line ratios, physical parameters, and abundances

The values of the diagnostic line ratios, electron densities (N_e), and electron temperatures (T_e) for the selected regions and the integrated spectrum of Mrk 900 are shown in Table 6. The values of N_e and T_e were computed using the five-level atom FIVEL program in the IRAF NEBULAR package (De Robertis et al. 1987; Shaw & Dufour 1995). The electronic densities were estimated from the [S II] $\lambda 6717, 6731$ line ratio (Osterbrock & Ferland 2006); we found that all regions present values in the low-density regime; knot 5 has a slightly higher density, close to 100 cm^{-3} . Where the [O III] $\lambda 4363$ line could be measured (knots 1, 3, and 5) we derived the electron temperature from the [O III] $\lambda 4363 / (\lambda 4959 + \lambda 5007)$ line ratio.

The oxygen abundance could not be determined using the direct T_e method (not even in the three knots where [O III] $\lambda 4363$ was measured) because this method requires the measurement of the [O II] $\lambda 3727 + 3729$ line, which unfortunately falls out of the VIMOS spectral range. Alternatively, the auroral [O II] $\lambda 7320, 7330$ lines could be used, but for Mrk 900 these features fall very close to the edge of the VIMOS spectrum in a zone that is highly affected by sky residuals, which prevents us from obtaining reliable flux values. We therefore estimated the oxygen abundances by adopting the empirical method introduced by Pilyugin & Grebel (2016), which utilizes the intensities of the strong lines [O III] $\lambda 4957, 5007$, [N II] $\lambda 6548, 6584$, and [S II] $\lambda 6717, 6731$. This calibrator provides (as usual) separate relations for high-metallicity and low-metallicity objects, but this degeneration can be simply broken using the N_2 line ratio ($N_2 = [\text{N II}] \lambda 6548, 6584 / \text{H}\beta$). For Mrk 900, all the measured spectra (i.e., the SF regions and the nuclear and integrated spectra) lie in the upper branch of the calibrator; the division between the upper and lower branches takes place at $\log N_2 = -0.6$. The relative accuracy of the abundance derived using this method is 0.1 dex.

The oxygen abundances are similar in all the knots and the integrated spectrum, $12 + \log(\text{O}/\text{H}) \sim 8.25$ ($\approx 0.3 Z_\odot^3$); this value is slightly higher than that found by Zhao et al. (2010) applying the direct- T_e method, $12 + \log(\text{O}/\text{H}) = 8.07 \pm 0.03$. Nearly homogeneous chemical abundances have been found for most of the blue compact and dwarf irregular galaxies investigated so

far (Croxall et al. 2009; Haurberg et al. 2013; Lagos et al. 2014, 2016; Cairós & González-Pérez 2017a,b).

4. Discussion

The results derived in the previous section make it possible to investigate the star-forming history (SFH) and the SF process in Mrk 900. The first step used to probe the SFH in a galaxy is to disentangle its stellar populations; it is already difficult to work with galaxies that cannot be resolved into stars, and this task becomes particularly tricky when we deal with starburst objects. IFS observations, supplying a broad set of observables for every element of spatial resolution, provide a novel and powerful way to approach the problem (Cairós & González-Pérez 2017a,b).

Combining our VIMOS/IFU and broad-band imaging data we distinguish at least two stellar populations in Mrk 900: a very young component (exposed in the emission-line maps) and a significantly older stellar population (traced to large galactocentric distances in the broad-band pictures). We can constrain the properties of these different stellar populations by comparing the derived observables with the predictions of evolutionary synthesis models.

We focus first on the very young stars. Only O and early B stars, with temperatures higher than $30,000 \text{ K}$ and masses above $10 M_\odot$, produce photons with energy high enough to ionize hydrogen. Models show that these stars evolve quickly: ionizing stars cannot be older than 10 Myr (Leitherer & Heckman 1995; Ekström et al. 2012; Langer 2012). Hence, the star clusters generating the H II regions in the central parts of Mrk 900 are younger than 10 Myr.

The H α flux in the whole mapped area (derived from the summed spectrum) is $5.7 \pm 0.03 \times 10^{-13} \text{ erg s}^{-1} \text{ cm}^{-2}$, consistent with the value $5.5 \pm 0.6 \times 10^{-13} \text{ erg s}^{-1} \text{ cm}^{-2}$ reported by Gil de Paz et al. (2003) from narrow-band images. From the total luminosity $L(\text{H}\alpha) = 2.4 \times 10^{40} \text{ erg s}^{-1}$, we derive a $\text{SFR} = 0.17 \pm 0.02 M_\odot \text{ yr}^{-1}$, applying the following expression from Hunter et al. (2010):

$$\text{SFR}(M_\odot \text{ yr}^{-1}) = 6.9 \times 10^{-42} L_{\text{H}\alpha}(\text{erg s}^{-1}).$$

This formula, derived in Kennicutt (1998), was modified for a subsolar metallicity, which is the most appropriate for dwarf galaxies. The derived SFR is slightly higher than the value $0.12 M_\odot \text{ yr}^{-1}$ reported in Hunt et al. (2015)⁴.

To compare this SFR with those of other galaxies, we must take into account the galaxy size (see discussion in Hunter & Elmegreen 2004). Normalizing the SFR to the radio at surface brightness level 25 mag arcsec⁻² (R_{25}) we obtain $\text{SFR} = 0.0105 M_\odot \text{ yr}^{-1} \text{ kpc}^{-2}$, a substantially high SFR even among the BCG class; for a sample of 23 BCGs, Hunter & Elmegreen (2004) reported an average SFR of $0.0062 M_\odot \text{ yr}^{-1} \text{ kpc}^{-2}$.

The global SFR ($0.17 \pm 0.02 M_\odot \text{ yr}^{-1}$) and the mass of atomic hydrogen ($M_{\text{HI}} = 1.55 \times 10^8 M_\odot$; van Zee et al. 2001) imply a depletion time (the timescale to exhaust the current gas supply of the galaxy; Roberts 1963) $\tau = 0.9 \text{ Gyr}$. According to the classical definition, this classifies Mrk 900 as a starburst galaxy, i.e., a galaxy whose “SFR cannot be sustained for a significant fraction of the Hubble time with the available interstellar gas” (Gallagher 2005; Heckman 2005; McQuinn et al. 2010).

⁴ The SFR in Hunt et al. (2015) is derived using H α and $24 \mu\text{m}$ following Calzetti et al. (2010).

³ With solar abundance, $12 + \log(\text{O}/\text{H}) = 8.69$ (Asplund et al. 2009)

Table 4. $H\alpha$ derived quantities for the major SF regions identified in Mrk 900.

Knot	$F(H\alpha)$ (10^{-16} erg cm $^{-2}$ s $^{-1}$)	$\log[L(H\alpha)]$ (erg s $^{-1}$)	SFR M \odot yr $^{-1}$	$W(H\alpha)$ (Å)	Age (Myr)
1	1602 \pm 37	39.83 \pm 0.14	0.047 \pm 0.007	214	5.5
2	95 \pm 14	38.61 \pm 0.20	0.0028 \pm 0.0006	94	6.3
3	95 \pm 11	38.61 \pm 0.18	0.0028 \pm 0.0006	78	6.5
4	32 \pm 6	38.13 \pm 0.23	0.0009 \pm 0.0002	77	6.5
5	382 \pm 186	39.21 \pm 0.51	0.011 \pm 0.006	73	6.6
6	118 \pm 6	38.70 \pm 0.15	0.0035 \pm 0.0005	78	6.5
7	147 \pm 9	38.80 \pm 0.15	0.0043 \pm 0.0006	107	6.2

Note: $H\alpha$ fluxes were corrected from interstellar extinction using the values provided in Table 5

The $H\alpha$ fluxes, luminosities, and equivalent widths of the individual H II regions identified in Mrk 900 (see Section 3.7) are shown in Table 4. To constrain their properties, we compare the $H\alpha$ equivalent widths with the predictions of the STARBURST 99 evolutionary synthesis models (Leitherer et al. 1999). Adopting the models with metallicity $Z=0.008$ (the value closest to the metallicity derived from the emission-line fluxes) we find that we can reproduce the measured equivalent widths with an instantaneous burst of SF, a Salpeter IMF with an upper mass limit of 100 M \odot , and ages ranging from 5.5 to 6.6 Myr. This age range must be understood, however, as an upper limit: the measured equivalent widths can decrease as a result of absorption from A-F stars and/or dilution due to the continuum from an older stellar population (Fernandes et al. 2003; Levesque & Leitherer 2013). We corrected the $H\alpha$ measurements in Table 4 for stellar absorption (see Section 2.2.1), but no attempt was made to correct for the presence of the older stars; the uncertainties in the ages of the SF knots due to the contribution from an older population were estimated by Cairós et al. (2002, 2007) to be up to ~ 1 -1.5 Myr.

The ionized gas emission is manifestly dominated by knot 1: it generates $\sim 30\%$ of the total $H\alpha$ flux in the observed area. With a $H\alpha$ luminosity of $6.84 \pm 0.9 \times 10^{39}$ ergs $^{-1}$ and a diameter about 300 pc, knot 1 is classified as a giant extragalactic H II region (GEHR). It is, indeed, comparable in size with the 30 Doradus nebula, the largest GEHR in the Local Group. The detection of the WR bump in this knot provides an independent age estimation of 3-6 Myr (Schaerer & Vacca 1998), consistent with that derived from $H\alpha$.

The morphology of the central starburst region in the continuum (Figure 2) strongly differs from the morphology in emission lines (Figures 5-8). From the seven H II regions identified in emission lines, only knot 1 has a visible counterpart in the continuum (knot a); however, it appears only as a moderate continuum emitter. The continuum maximum (knot c), located about the center of the elliptical host, is about 130 pc southwest from its nearest H II region (knot 5). Such morphological patterns may indicate the presence of distinct bursts of SF and spatial migration of the SF sites (Petrosian et al. 2002). By carrying out similar IFU analyses in the BCGs Haro 14 and Tololo 1937-423, we identified two temporally and spatially separated bursts whose ages suggest a scenario of triggered SF (Cairós & González-Pérez 2017a,b). In Mrk 900, however, the presence of a second episode of SF cannot be definitely confirmed, as knot c could be also the nucleus of the host component and the increase in intensity the result of a higher stellar density. The high values of the $H\gamma$ and $H\beta$ equivalent widths in absorption ($\sim 5\text{Å}$) in the nuclear spectrum might indicate the presence of intermediate-age stars, but the possibility that such large equivalent widths originate in the nearby H II regions and/or are

due to a strong dilution in the continuum peak cannot be ruled out.

We now focus on the properties of the galaxy host, very well traced in the NOT images. In the galaxy outskirts, we find no SF regions but a rather red and regularly shaped host, with elliptical isophotes. The outer regions of the SBP are well described by an exponential function; consistently, the velocity field indicates the presence of a rotating disk, although perturbed in the inner parts. The region covered by VIMOS is still heavily affected by the starburst, and we could not derive the rotation curve; however, from the velocity field we estimated a maximum velocity amplitude ~ 80 -90 km sec $^{-1}$ along the optical major axis. This value is in very good agreement with the velocity 82.0 km sec $^{-1}$ at a distance of ~ 1 kpc reported by van Zee et al. (2001) from H I data.

A comparison of the colors of the host galaxy with the predictions of evolutionary synthesis models (Vazdekis et al. 1996, 2010; Fioc & Rocca-Volmerange 1997; Le Borgne et al. 2004) suggests ages of several Gyr. Thus, the morphology, structure, dynamics, and age of the host galaxy are similar to those presented by dE galaxies (Lin & Faber 1983; van Zee et al. 2004b,a).

In summary, we identified in Mrk 900 a very young population (≤ 6.6 Myr) resolved in an ensemble of H II regions and extending about 1 kpc along the galaxy minor axis. This young component presents a rather distorted appearance in emission lines, with multiple filamentary and bubble-like structures. Underlying the young stars there is an old (several Gyr) stellar population with smooth elliptical isophotes, which extends up to radius of 4 kpc.

What mechanism has ignited the actual SF burst in Mrk 900 after (most probably) several Gyr of inactivity is not evident. The nature of the starburst trigger in low-mass systems has been (and is still) widely debated (Pustilnik et al. 2001; Brosch et al. 2004). Several internal processes have been discussed, for example stochastic self propagating star formation (SSPSF, Gerola et al. 1980) or torques in spiral disk clumps (Elmegreen et al. 2012). However, an increasing amount of observations suggests that external triggers, such as interactions and mergers (Brinks 1990; Taylor et al. 1996; Östlin et al. 2001; Pustilnik et al. 2001; Ekta et al. 2008; Lelli et al. 2014) or external gas infalling (López-Sánchez et al. 2012; Nidever et al. 2013; Ashley et al. 2014; Miura et al. 2015; Turner et al. 2015) play a major role in the ignition of the starburst in BCGs. These observational results are strengthened by numerical simulations that successfully reproduce the merger (Bekki 2008) or gas infall scenario (Verbeke et al. 2014).

The observational evidence speaks against interactions or mergers with a massive galaxy as being responsible for the present-day SF in Mrk 900: in the HYPERLEDA database the galaxy appears classified as “isolated” (i.e., it does not have bright neighboring objects); the LSB component shows a very regular behavior, without tidal features or any other sign of asymmetry, in the optical and NIR (Section 3.2 and Micheva et al. 2013a; Janowiecki & Salzer 2014); the distortion of the isophotes in the central area is clearly due to the superposition of the SF episode; the velocity field is relatively smooth out of the starburst regions, both in the optical (Section 3.6) and in radio (van Zee et al. 2001); finally, we did not find any significant metallicity variations among the individual stellar clusters (Section 3.7).

On the other hand, interactions with low-mass companions, mergers between gas-rich dwarf galaxies or external gas infalling are all triggering scenarios consistent with our results: a centrally concentrated SF, as we observe in Mrk 900, is expected after an interaction/merger event; a collision can drive mass inflows to the galaxy central regions and ignite a nuclear starburst (Mihos & Hernquist 1994; Bekki 2008); the alignment of the SF with the galaxy minor axis points to inflowing (generated in a collision) or outflowing gas, but the two scenarios are rather difficult to distinguish observationally. The presence of shocked and high velocity-dispersion regions (Section 3.6; Section 3.5) and the substantial amount of dust (Fig. 9) is also suggestive of an interaction or accretion event.

In addition, the H I synthesis observations of Mrk 900 presented in van Zee et al. (2001) reveal an extended and distorted morphology. The galaxy neutral gas distribution shows clear deviations from symmetry in the outer regions, the most evident being two extensions departing toward the east and northeast (Fig. 6 in van Zee et al. 2001). More recent work, dealing with higher sensitivity and spatial resolution observations on nearby starbursting dwarfs, have resolved such distorted H I morphologies into different components, for example tails, plumes, or clouds (IC 10, Ashley et al. 2013; Nidever et al. 2013; NGC 5253, Kobulnicky & Skillman 2008; López-Sánchez et al. 2012 or NGC 1569, Johnson et al. 2012; Johnson 2013), and interpreted these findings as evidence of interactions or inflowing gas. In the case of BCG NGC 5253, the infall scenario is further supported by kinematic CO observations (Miura et al. 2015; Turner et al. 2015).

5. Summary and conclusions

This work presents results on a spectrophotometric analysis of the BCG Mrk 900, carried out by combining VIMOS/IFU observations with deep (BVR) broad-band imaging. From the IFU data we built continuum, emission-line, and diagnostic line ratio maps, and generated LOS velocity and velocity dispersion maps of the central starburst region. Using the broad-band frames, which trace the underlying stellar host, we derived SBPs and color maps.

From our analysis we highlight the following results:

- We disentangled two stellar components in Mrk 900: an ionizing (very young) population, resolved in individual stellar clusters and extending about 1 kpc along the galaxy minor axis, and a very regular LSB stellar host, which reaches galactocentric distances up to ~ 4 kpc and exhibits red colors, consistent with ages of several Gyr.
- We generated the integrated spectrum of the major seven H II regions identified in Mrk 900, and of its nuclear region.

From these spectra we derived reliable physical parameters and oxygen abundances. We found, for all knots, similar values of the abundance, $12+\log(\text{O}/\text{H}) \sim 8.25$ ($\approx 0.3 Z_{\odot}$), and no evidence of metallicity variations. Using evolutionary synthesis models we estimated ages of 5.5–6.6 Myr for all the ionizing clusters. We detected in the larger H II region (knot 1) the WR bump at $\lambda 4650 - 4690 \text{ \AA}$, and therefore we demonstrated that Mrk 900 can be classified as a WR galaxy.

- We showed that Mrk 900 contains a substantial amount of dust, with $A_V \geq 0.48$ in the whole mapped area. The dust distribution is inhomogeneous, with a dust lane crossing the central starburst northeast–southwest; dust lanes and patches are also distinguished in the broad-band frames and color map.

- Diagnostic maps and diagnostic diagrams have shown the presence of shock-dominated zones in Mrk 900; these regions are situated primarily at the periphery of the mapped (starburst) area and in the inter-knot region, conforming with the idea of shocks being generated in the interface between expanding bubbles (generated by the massive stars) and the ambient ISM.

- We built velocity and velocity dispersion fields from the brightest emission lines. Although deviation from circular motions is evident, the galaxy displays an overall rotation pattern. The dispersion map is inhomogeneous, and the areas of higher dispersion coincide spatially with the areas of low surface brightness.

- Given our observational results, we argue that an interaction with a low-mass system, a merger between gas-rich dwarf galaxies, or infalling from external gas clouds are all plausible scenarios for the ignition of the actual burst of SF in Mrk 900.

Table 5. Reddening-corrected line intensity ratios, normalized to $H\beta$, for the SF knots and the nuclear region in Mrk 900.

Ion	knot 1	Knot 2	Knot 3	Knot 4	Knot 5	Knot 6	Knot 7	Nuc	Sum
4340 $H\gamma$	0.482±0.004	0.434±0.020	0.589±0.029	0.498±0.042	0.494±0.009	0.474±0.016	0.485±0.019	0.498±0.011	0.493±0.003
4363 [OIII]	0.021±0.002	—	0.037±0.013	—	0.045±0.012	—	—	—	—
4472 HeI	0.038±0.002	—	—	—	0.034±0.008	—	—	—	—
4861 $H\beta$	1.000	1.000	1.000	1.000	1.000	1.000	1.000	1.000	1.000
4959 [OIII]	1.043±0.006	0.930±0.030	0.834±0.028	0.751±0.039	0.958±0.014	0.608±0.013	0.696±0.016	0.825±0.012	0.791±0.003
5007 [OIII]	3.091±0.016	2.771±0.074	2.534±0.062	2.288±0.088	2.864±0.031	1.794±0.030	2.047±0.034	2.509±0.030	2.401±0.007
5875 HeI	0.102±0.002	0.098±0.021	0.088±0.013	0.093±0.032	0.088±0.006	—	0.085±0.007	0.091±0.007	—
6300 [OI]	0.024±0.001	0.070±0.014	0.097±0.009	—	0.050±0.005	0.066±0.008	0.077±0.007	0.056±0.006	—
6548 [NII]	0.074±0.001	0.088±0.011	0.130±0.012	0.137±0.037	0.103±0.004	0.124±0.007	0.126±0.007	0.118±0.006	0.135±0.002
6563 $H\alpha$	2.870±0.020	2.870±0.104	2.870±0.095	2.870±0.146	2.870±0.043	2.870±0.060	2.870±0.061	2.870±0.047	2.870±0.012
6584 [NII]	0.226±0.002	0.270±0.015	0.403±0.017	0.404±0.032	0.337±0.008	0.381±0.012	0.385±0.011	0.367±0.008	0.361±0.002
6678 HeI	0.030±0.001	—	—	—	0.022±0.005	—	0.025±0.007	—	—
6717 [SII]	0.238±0.003	0.354±0.018	0.585±0.024	0.541±0.040	0.375±0.008	0.487±0.014	0.496±0.013	0.438±0.009	0.477±0.002
6731 [SII]	0.170±0.002	0.241±0.014	0.386±0.017	0.369±0.032	0.282±0.006	0.336±0.011	0.354±0.011	0.324±0.008	0.339±0.002
7136 [ArIII]	0.097±0.002	0.083±0.012	0.090±0.011	0.097±0.023	0.096±0.004	—	0.086±0.008	0.091±0.006	—
$F_{H\beta}$	558±13	30±4	33±4	11±2	133±65	41±2	51±3	16±1	1997±24
$C_{H\beta}$	0.439±0.006	0.467±0.030	0.434±0.028	0.398±0.042	0.439±0.012	0.288±0.017	0.317±0.018	0.418±0.014	0.408±0.004
$W(H\gamma)_{ab}$	2.1	—	3.4	—	3.7	—	1.9	5.0	2.5
$W(H\beta)_{ab}$	1.9	2.2	3.3	—	4.5	2.4	3.7	5.1	3.5
A_V	0.945±0.012	1.012±0.065	0.938±0.058	0.860±0.092	0.948±0.027	0.623±0.038	0.685±0.038	0.904±0.030	0.882±0.007
$E(B-V)$	0.306±0.004	0.326±0.021	0.302±0.019	0.278±0.029	0.306±0.009	0.201±0.012	0.221±0.012	0.292±0.009	0.284±0.002

Notes. Reddening-corrected line fluxes normalized to $F(H\beta)=1$. The reddening-corrected $H\beta$ flux (in units of $10^{-16}\text{erg s}^{-1}\text{cm}^{-2}$), the interstellar extinction coefficient $C_{H\beta}$, and the values of the equivalent width in absorption for $H\gamma$ and $H\beta$ (in Å) are also provided in the table. $A_V=2.16\times C(H\beta)$ and $E(B-V)=0.697\times C(H\beta)$ (Dopita & Sutherland 2003).

Table 6. Line ratios, physical parameters, and abundances.

Parameter	Knot 1	Knot 2	Knot 3	Knot 4	Knot 5	Knot 6	Knot 7	Nuclear	Integrated
[O III] $\lambda 5007/\text{H}\beta$	3.091 \pm 0.094	2.784 \pm 0.573	2.534 \pm 0.371	2.280 \pm 0.469	2.864 \pm 0.190	1.794 \pm 0.115	2.047 \pm 0.142	2.508 \pm 0.175	2.401 \pm 0.040
[O I] $\lambda 6300/\text{H}\alpha$	0.008 \pm 0.001	0.021 \pm 0.004	0.034 \pm 0.004	—	0.017 \pm 0.002	0.023 \pm 0.003	0.027 \pm 0.003	0.019 \pm 0.002	—
[N II] $\lambda 6584/\text{H}\alpha$	0.079 \pm 0.001	0.092 \pm 0.010	0.140 \pm 0.011	0.141 \pm 0.017	0.118 \pm 0.004	0.133 \pm 0.006	0.134 \pm 0.005	0.128 \pm 0.005	0.126 \pm 0.001
[S II] $\lambda\lambda 6717\ 6731/\text{H}\alpha$	0.142 \pm 0.002	0.202 \pm 0.169	0.338 \pm 0.021	0.317 \pm 0.031	0.229 \pm 0.007	0.287 \pm 0.010	0.296 \pm 0.010	0.266 \pm 0.008	0.285 \pm 0.002
N_e (cm $^{-3}$)	<100	<100	<100	<100	\approx 100	<100	<100	<100	<100
T_e (K)	10236	—	13450	—	13840	—	—	—	—
12+log(O/H) 2	8.23	8.21	8.24	8.26	8.25	8.25	8.25	8.25	8.25

Notes. Abundances are derived following Pilyugin & Grebel (2016).

Acknowledgements. L.M. Cairós acknowledges support from the Deutsche Forschungsgemeinschaft (CA 1243/1-1 and CA 1243/1-2). We thank Rafael Manso Sainz for extremely stimulating discussions and a careful reading of the manuscript. The data presented here were obtained [in part] with ALFOSC, which is provided by the Instituto de Astrofísica de Andalucía (IAA) under a joint agreement with the University of Copenhagen and NOTSA. This research has made use of the NASA/IPAC Extragalactic Database (NED), which is operated by the Jet Propulsion Laboratory, Caltech, under contract with the National Aeronautics and Space Administration. We acknowledge the usage of the HyperLeda database (<http://leda.univ-lyon1.fr>).

References

- Allen, M. G., Groves, B. A., Dopita, M. A., Sutherland, R. S., & Kewley, L. J. 2008, *ApJS*, 178, 20
- Ashley, T., Elmegreen, B. G., Johnson, M., et al. 2014, *AJ*, 148, 130
- Ashley, T., Simpson, C. E., & Elmegreen, B. G. 2013, *AJ*, 146, 42
- Asplund, M., Grevesse, N., Sauval, A. J., & Scott, P. 2009, *ARA&A*, 47, 481
- Baldwin, J. A., Phillips, M. M., & Terlevich, R. 1981, *PASP*, 93, 5
- Bekki, K. 2008, *MNRAS*, 388, L10
- Blanc, G. A., Heiderman, A., Gebhardt, K., Evans, N. J., & Adams, J. 2009, *ApJ*, 704, 842
- Bomans, D. J., Chu, Y.-H., & Hopp, U. 1997, *AJ*, 113, 1678
- Bomans, D. J., van Eymeren, J., Dettmar, R.-J., Weis, K., & Hopp, U. 2007, *New A Rev.*, 51, 141
- Bordalo, V., Plana, H., & Telles, E. 2009, *ApJ*, 696, 1668
- Brinks, E. 1990, II Zwicky 33: star formation induced by a recent interaction., ed. Wielen, R., 146–149
- Brosch, N., Almozino, E., & Heller, A. B. 2004, *MNRAS*, 349, 357
- Cairós, L. M., Caon, N., García-Lorenzo, B., et al. 2012, *A&A*, 547, A24
- Cairós, L. M., Caon, N., García-Lorenzo, B., et al. 2007, *ApJ*, 669, 251
- Cairós, L. M., Caon, N., García-Lorenzo, B., Vílchez, J. M., & Muñoz-Tuñón, C. 2002, *ApJ*, 577, 164
- Cairós, L. M., Caon, N., Papaderos, P., et al. 2009a, *ApJ*, 707, 1676
- Cairós, L. M., Caon, N., Vílchez, J. M., González-Pérez, J. N., & Muñoz-Tuñón, C. 2001a, *ApJS*, 136, 393
- Cairós, L. M., Caon, N., & Weilbacher, P. M. 2015, *A&A*, 577, A21
- Cairós, L. M., Caon, N., Zurita, C., et al. 2010, *A&A*, 520, A90+
- Cairós, L. M., Caon, N., Zurita, C., et al. 2009b, *A&A*, 507, 1291
- Cairós, L. M. & González-Pérez, J. N. 2017a, *A&A*, 600, A125
- Cairós, L. M. & González-Pérez, J. N. 2017b, *A&A*, 608, A119
- Cairós, L. M., Vílchez, J. M., González Pérez, J. N., Iglesias-Páramo, J., & Caon, N. 2001b, *ApJS*, 133, 321
- Calzetti, D., Conelice, C. J., Gallagher, John S., I., & Kinney, A. L. 1999, *The Astronomical Journal*, 118, 797
- Calzetti, D., Harris, J., Gallagher, John S., I., et al. 2004, *The Astronomical Journal*, 127, 1405
- Calzetti, D., Wu, S.-Y., Hong, S., et al. 2010, *ApJ*, 714, 1256
- Caon, N., Cairós, L. M., Aguerri, J. A. L., & Muñoz-Tuñón, C. 2005, *ApJS*, 157, 218
- Conti, P. S. 1991, *ApJ*, 377, 115
- Croxall, K. V., van Zee, L., Lee, H., et al. 2009, *ApJ*, 705, 723
- De Robertis, M. M., Dufour, R. J., & Hunt, R. W. 1987, *JRASC*, 81, 195
- de Vaucouleurs, G., de Vaucouleurs, A., Corwin, Jr., H. G., et al. 1991, *Third Reference Catalogue of Bright Galaxies*, ed. de Vaucouleurs, G., de Vaucouleurs, A., Corwin, H. G., Jr., Buta, R. J., Paturel, G., & Fouque, P.
- Dekel, A. & Silk, J. 1986, *ApJ*, 303, 39
- Dopita, M. A. & Sutherland, R. S. 2003, *Astrophysics of the diffuse universe* Dottori, H. A. 1981, *Ap&SS*, 80, 267
- Doublier, V., Caulet, A., & Comte, G. 1999, *A&AS*, 138, 213
- Doublier, V., Comte, G., Petrosian, A., Surace, C., & Turatto, M. 1997, *A&AS*, 124, 405
- Ekström, S., Georgy, C., Eggenberger, P., et al. 2012, *A&A*, 537, A146
- Ekta, Chingalur, J. N., & Pustilnik, S. A. 2008, *MNRAS*, 391, 881
- Elmegreen, B. G., Zhang, H.-X., & Hunter, D. A. 2012, *ApJ*, 747, 105
- Fanelli, M. N., O’Connell, R. W., & Thuan, T. X. 1988, *ApJ*, 334, 665
- Fernandes, R. C., Leão, J. R. S., & Lacerda, R. R. 2003, *MNRAS*, 340, 29
- Fioc, M. & Rocca-Volmerange, B. 1997, *A&A*, 326, 950
- Flores-Fajardo, N., Morisset, C., & Binette, L. 2009, *Rev. Mexicana Astron. Astrofis.*, 45, 261
- Gallagher, John S., I. 2005, in *Astrophysics and Space Science Library*, Vol. 329, *Starbursts: From 30 Doradus to Lyman Break Galaxies*, ed. R. de Grijs & R. M. González Delgado, 11
- Gerola, H., Seiden, P. E., & Schulman, L. S. 1980, *ApJ*, 242, 517
- Gil de Paz, A. & Madore, B. F. 2005, *ApJS*, 156, 345
- Gil de Paz, A., Madore, B. F., & Pevunova, O. 2003, *ApJS*, 147, 29
- González Delgado, R. M. & Leitherer, C. 1999, *ApJS*, 125, 479
- González Delgado, R. M., Leitherer, C., & Heckman, T. M. 1999, *ApJS*, 125, 489
- Guseva, N. G., Izotov, Y. I., & Thuan, T. X. 2000, *ApJ*, 531, 776
- Haurberg, N. C., Rosenberg, J., & Salzer, J. J. 2013, *ApJ*, 765, 66
- Heckman, T. M. 2005, in *Astrophysics and Space Science Library*, Vol. 329, *Starbursts: From 30 Doradus to Lyman Break Galaxies*, ed. R. de Grijs & R. M. González Delgado, 3
- Hong, S., Calzetti, D., Gallagher, III, J. S., et al. 2013, *ApJ*, 777, 63
- Hunt, L. K., García-Burillo, S., Casasola, V., et al. 2015, *A&A*, 583, A114
- Hunt, L. K., Weiß, A., Henkel, C., et al. 2017, *A&A*, 606, A99
- Hunter, D. 1997, *PASP*, 109, 937
- Hunter, D. A. & Elmegreen, B. G. 2004, *AJ*, 128, 2170
- Hunter, D. A., Elmegreen, B. G., & Ludka, B. C. 2010, *AJ*, 139, 447
- Hunter, D. A. & Gallagher, III, J. S. 1990, *ApJ*, 362, 480
- Izotov, Y. I. & Thuan, T. X. 1999, *ApJ*, 511, 639
- Janowiecki, S. & Salzer, J. J. 2014, *ApJ*, 793, 109
- Jedrzejewski, R. I. 1987, *MNRAS*, 226, 747
- Johnson, M. 2013, *AJ*, 145, 146
- Johnson, M., Hunter, D. A., Oh, S.-H., et al. 2012, *AJ*, 144, 152
- Kauffmann, G., Heckman, T. M., Tremonti, C., et al. 2003, *MNRAS*, 346, 1055
- Kennicutt, Jr., R. C. 1998, *ARA&A*, 36, 189
- Kewley, L. J., Dopita, M. A., Sutherland, R. S., Heisler, C. A., & Trevena, J. 2001, *ApJ*, 556, 121
- Kobulnicky, H. A. & Skillman, E. D. 2008, *AJ*, 135, 527
- Kumari, N., James, B. L., & Irwin, M. J. 2017, *MNRAS*, 470, 4618
- Kunth, D. & Östlin, G. 2000, *A&A Rev.*, 10, 1
- Lacerda, E. A. D., Cid Fernandes, R., Couto, G. S., et al. 2018, *MNRAS*, 474, 3727
- Lagos, P., Demarco, R., Papaderos, P., et al. 2016, *MNRAS*, 456, 1549
- Lagos, P., Papaderos, P., Gomes, J. M., Smith Castelli, A. V., & Vega, L. R. 2014, *A&A*, 569, A110
- Landolt, A. U. 1992, *AJ*, 104, 340
- Langer, N. 2012, *ARA&A*, 50, 107
- Le Borgne, D., Rocca-Volmerange, B., Prugniel, P., et al. 2004, *A&A*, 425, 881
- Le Fèvre, O., Saisse, M., Mancini, D., et al. 2003, *Society of Photo-Optical Instrumentation Engineers (SPIE) Conference Series*, Vol. 4841, *Commissioning and performances of the VLT-VIMOS instrument*, ed. M. Iye & A. F. M. Moorwood, 1670–1681
- Lebouteiller, V., Péquignot, D., Cormier, D., et al. 2017, *A&A*, 602, A45
- Leitherer, C. 2005, in *American Institute of Physics Conference Series*, Vol. 783, *The Evolution of Starbursts*, ed. S. Hüttmeister, E. Manthey, D. Bomans, & K. Weis, 280–295
- Leitherer, C. & Heckman, T. M. 1995, *ApJS*, 96, 9
- Leitherer, C., Schaerer, D., Goldader, J. D., et al. 1999, *ApJS*, 123, 3
- Lelli, F., Verheijen, M., & Fraternali, F. 2014, *MNRAS*, 445, 1694
- Leslie, S. K., Rich, J. A., Kewley, L. J., & Dopita, M. A. 2014, *MNRAS*, 444, 1842
- Levesque, E. M. & Leitherer, C. 2013, *ApJ*, 779, 170
- Lin, D. N. C. & Faber, S. M. 1983, *ApJ*, 266, L21
- López-Sánchez, Á. R., Koribalski, B. S., van Eymeren, J., et al. 2012, *MNRAS*, 419, 1051
- Mac Low, M.-M. & Ferrara, A. 1999, *ApJ*, 513, 142
- Madden, S. C., Galliano, F., Jones, A. P., & Sauvage, M. 2006, *A&A*, 446, 877
- Madden, S. C., Rémy-Ruyer, A., Galametz, M., et al. 2013, *PASP*, 125, 600
- Marlowe, A. T., Heckman, T. M., Wyse, R. F. G., & Schommer, R. 1995, *ApJ*, 438, 563
- Martin, C. L. 1998, *ApJ*, 506, 222
- Martin, C. L. 1999, *ApJ*, 513, 156
- Mazzarella, J. M. & Balzano, V. A. 1986, *ApJS*, 62, 751
- McCall, M. L., Rybski, P. M., & Shields, G. A. 1985, *ApJS*, 57, 1
- McCray, R. & Kafatos, M. 1987, *ApJ*, 317, 190
- McQuinn, K. B. W., Skillman, E. D., Cannon, J. M., et al. 2010, *ApJ*, 721, 297
- Meynet, G. 1995, *A&A*, 298, 767
- Micheva, G., Östlin, G., Bergvall, N., et al. 2013a, *MNRAS*, 431, 102
- Micheva, G., Östlin, G., Zackrisson, E., et al. 2013b, *A&A*, 556, A10
- Mihos, J. C. & Hernquist, L. 1994, *ApJ*, 425, L13
- Mingozzi, M., Cresci, G., Venturi, G., et al. 2019, *A&A*, 622, A146
- Miura, R. E., Espada, D., Sugai, H., Nakanishi, K., & Hirota, A. 2015, *PASJ*, 67, L1
- Moiseev, A. V. & Lozinskaya, T. A. 2012, *MNRAS*, 423, 1831
- Moiseev, A. V., Tikhonov, A. V., & Klypin, A. 2015, *MNRAS*, 449, 3568
- Nelson, A. H. & Matsuda, T. 1977, *MNRAS*, 179, 663
- Nidever, D. L., Ashley, T., Slater, C. T., et al. 2013, *ApJ*, 779, L15
- Noeske, K. G., Papaderos, P., Cairós, L. M., & Fricke, K. J. 2003, *A&A*, 410, 481
- Noeske, K. G., Papaderos, P., Cairós, L. M., & Fricke, K. J. 2005, *A&A*, 429, 115
- O’Donnell, J. E. 1994, *ApJ*, 422, 158

- Oey, M. S., Meurer, G. R., Yelda, S., et al. 2007, *ApJ*, 661, 801
- Olofsson, K. 1995, *A&AS*, 111, 57
- Osterbrock, D. E. & Ferland, G. J. 2006, *Astrophysics of gaseous nebulae and active galactic nuclei* (Astrophysics of gaseous nebulae and active galactic nuclei, 2nd. ed. by D.E. Osterbrock and G.J. Ferland. Sausalito, CA: University Science Books, 2006)
- Östlin, G., Amram, P., Bergvall, N., et al. 2001, *A&A*, 374, 800
- Papaderos, P., Izotov, Y. I., Thuan, T. X., et al. 2002, *A&A*, 393, 461
- Papaderos, P., Loose, H.-H., Thuan, T. X., & Fricke, K. J. 1996, *A&AS*, 120, 207
- Petrosian, A. R., Movsessian, T., Comte, G., Kunth, D., & Dodonov, S. 2002, *A&A*, 391, 487
- Pilyugin, L. S. & Grebel, E. K. 2016, *MNRAS*, 457, 3678
- Pustilnik, S. A., Kniazev, A. Y., Lipovetsky, V. A., & Ugryumov, A. V. 2001, *A&A*, 373, 24
- Reynolds, R. J., Scherb, F., & Roesler, F. L. 1973, *ApJ*, 185, 869
- Rich, J. A., Kewley, L. J., & Dopita, M. A. 2011, *ApJ*, 734, 87
- Rich, J. A., Kewley, L. J., & Dopita, M. A. 2015, *ApJS*, 221, 28
- Rich, J. A., Torrey, P., Kewley, L. J., Dopita, M. A., & Rupke, D. S. N. 2012, *ApJ*, 753, 5
- Roberts, M. S. 1963, *ARA&A*, 1, 149
- Salzer, J. J., Rosenberg, J. L., Weisstein, E. W., Mazzarella, J. M., & Bothun, G. D. 2002, *AJ*, 124, 191
- Schaerer, D., Contini, T., & Pindao, M. 1999, *A&AS*, 136, 35
- Schaerer, D. & Vacca, W. D. 1998, *ApJ*, 497, 618
- Schlafly, E. F. & Finkbeiner, D. P. 2011, *ApJ*, 737, 103
- Seigar, M. S. & James, P. A. 2002, *MNRAS*, 337, 1113
- Sharp, R. G. & Bland-Hawthorn, J. 2010, *ApJ*, 711, 818
- Shaw, R. A. & Dufour, R. J. 1995, *PASP*, 107, 896
- Shu, F. H., Milione, V., Gebel, W., et al. 1972, *ApJ*, 173, 557
- Stasińska, G. & Leitherer, C. 1996, *ApJS*, 107, 661
- Taylor, C. L., Thomas, D. L., Brinks, E., & Skillman, E. D. 1996, *ApJS*, 107, 143
- Thuan, T. X., Lipovetsky, V. A., Martin, J.-M., & Pustilnik, S. A. 1999, *A&AS*, 139, 1
- Thuan, T. X. & Martin, G. E. 1981, *ApJ*, 247, 823
- Turner, J. L., Beck, S. C., Benford, D. J., et al. 2015, *Nature*, 519, 331
- van Zee, L., Barton, E. J., & Skillman, E. D. 2004a, *AJ*, 128, 2797
- van Zee, L., Salzer, J. J., & Skillman, E. D. 2001, *AJ*, 122, 121
- van Zee, L., Skillman, E. D., & Haynes, M. P. 2004b, *AJ*, 128, 121
- Vazdekis, A., Casuso, E., Peletier, R. F., & Beckman, J. E. 1996, *ApJS*, 106, 307
- Vazdekis, A., Sánchez-Blázquez, P., Falcón-Barroso, J., et al. 2010, *MNRAS*, 404, 1639
- Veilleux, S. & Osterbrock, D. E. 1987, *ApJS*, 63, 295
- Verbeke, R., De Rijcke, S., Koleva, M., et al. 2014, *MNRAS*, 442, 1830
- Zhao, Y., Gao, Y., & Gu, Q. 2010, *ApJ*, 710, 663